Database of storm-time equatorial ion temperatures in Earth's magnetosphere calculated from energetic neutral atom data and case studies showing "clearing" of hot ions from the plasma sheet

A. M. Keesee[1], R. M. Katus[2], M. Floyd[2], and E. E. Scime[3]

[1]Department of Physics & Astronomy and Space Science Center, University of New Hampshire, Durham, NH.

[2]Department of Mathematics, Eastern Michigan University, Ypsilanti, MI.

[3]Department of Physics & Astronomy, West Virginia University, Morgantown, WV.

Corresponding author: Amy Keesee (amy.keesee@unh.edu)

Key Points:

- Equatorial ion temperature maps have been calculated from ENA data at 10-minute time cadence for 2009-2017
- The database of temperature maps is available on CDAWeb
- Case studies of ion temperature drops concurrent with sharp negative IMF B_z gradients are presented

Abstract

Ion temperature is a key parameter that influences dynamics in the magnetosphere, such as particle transport and wave-particle interactions. Measurements of ion heating and energization yields information about phenomena such as magnetic reconnection, bursty bulk flows, and ion injections. Taking advantage of the global view provided by energetic neutral atom imaging, a database of ion temperature maps during geomagnetic storms occurring throughout the NASA TWINS mission has been created. These ion temperature maps and relevant metadata are publicly available on CDAWeb to facilitate comparison to in situ measurements and model output, for use as boundary conditions for simulations, and for other relevant studies. A preliminary study of average plasma sheet ion temperatures calculated from these maps has revealed a common occurrence of decreasing ion temperature concurrent with a sharp negative gradient in the IMF B_z. Two case studies are presented, supporting a hypothesis that substorm activity results in injection of high temperature ions, leaving behind an interval of lower plasma sheet temperatures.

Plain Language Summary

The Sun releases large chunks of energetic particles that can bombard the region of space surrounding Earth, causing an event called a geomagnetic storm. During these storms, particles can become heated and move around. We can measure the temperature of these particles to improve our understanding of what happens during these storms. We have made maps of such temperatures and are sharing them publicly so that others can use them in their own research. We have found some cases where the average temperature of space on the night-side of Earth decreases rapidly and remains low as if all of those hot particles were swept toward Earth and the particles left behind take a while to heat back up. This appears to be controlled by the magnetic field embedded in the chunks of energetic particles coming from the Sun.

1 Introduction

The terrestrial magnetosphere contains several distinct plasma populations: the plasmasphere, the ring current, the ionosphere, the radiation belts, and the plasma sheet. The plasma sheet is a layer of hot plasma that extends from the magnetotail into the inner magnetosphere. This region plays an important role in the transfer of energy from the solar wind to the Earth. The ion population in the plasma sheet influences the dynamics of the inner magnetosphere, especially during geomagnetically active intervals. Ions are convected or injected into the inner magnetosphere where they drive the ring current as well as waves that excite radiation belt particles (Ozeke & Mann, 2008; Takahashi, Seki, Amano, Miyoshi, & Yamakawa, 2019). Because of this, ion densities and temperatures are needed as boundary conditions for inner magnetosphere models.

Borovsky et al. (1998) demonstrated a correlation between solar wind speed and ion temperature in the plasma sheet; and recent studies showed a similar correlation between solar wind speed and enhancement of MeV electrons in the radiation belt (Zhao, Baker, Li, Jaynes, & Kanekal, 2019). The Tsyganenko & Mukai (2003) plasma sheet models are statistical models based on long-time averages of Geotail data that lack event-specific spatial and temporal variation (Elfritz, Keesee, Buzulukova, Fok, & Scime, 2014). Ion heating in the plasma sheet is associated with numerous phenomena including gradient-curvature drift (Spence & Kivelson, 1993), adiabatic heating, magnetic reconnection, and bursty bulk flows (BBF) (Angelopoulos,

Kennel, Kivelson, Walker, & Paschmann, 1992). Current modeling of the inner magnetosphere often involves coupling with a global magnetohydrodynamics (MHD) model. While these global models now have the ability to include transient events such as BBFs (e.g. Wiltberger, Merkin, Lyon, & Ohtani, 2015), it is unclear how well the temporal and spatial variation of the actual events are accurately modeled. Energetic neutral atom (ENA) imaging can provide a global view of the ion population to provide validation for MHD model results or be used directly for ion boundary conditions (Chen et al., 2015; Elfritz et al., 2014).

A dataset of ion temperature maps created from TWINS ENA measurements for storms over July 2009 - July 2015 was previously made available through NASA Space Physics Data Facility (SPDF) and described in Keesee & Scime (2015). However, that dataset was provided as IDL savesets without complete metadata, limiting its usability. We have expanded and improved upon that database. We now include all moderate and intense storms (Dst ≤ -60 nT) during July 2009-December 2017, increased the time cadence of the temperature maps to 10 minute averages, and increased the total interval analyzed for each storm to include four days, with the storm peak on the second day. This ensures that there is plenty of prestorm data, the entire main phase - the average main phase is 13.7 hours (Katus, Liemohn, Ionides, Ilie, & Welling, 2015)-, and two days of recovery. The new database is provided in Common Data Format (CDF) with critical metadata to make the dataset more readily available for use. Also included are arrays of the equatorial ENA flux used to calculate the ion temperatures. The dataset is archived at the NASA SPDF CDAWeb in a format compatible with the Virtual Observatory (VxO) architecture. In this paper, we describe that dataset and provide example analyses of the data.

2 Methodology

2.1 Storm selection

Geomagnetic storms of at least moderate intensity during the lifetime of the TWINS mission (July 2009-December 2017) are included in the database. They were selected using the Disturbance storm time (Dst) index from the Kyoto database with minimum Dst ≤ -60 nT. TWINS data with a 10-minute time cadence over a four-day window (starting the day prior to the day on which the minimum Dst occurred) were analyzed to provide pre-storm conditions as well as complete coverage of the main and recovery phases of the storm. A table of storms is provided in the supplemental material.

2.2 TWINS data and ion temperature analysis

The Two Wide-angle Imaging Neutral atom Spectrometers (TWINS) is a NASA Mission of Opportunity (McComas et al., 2009). TWINS is housed on two satellites in highly elliptical Molniya orbits with perigee of ~7 R_E that are alternating to provide near-continuous coverage. Each satellite contains an energetic neutral atom (ENA) imager, a Lyman-alpha detector, and in situ particle monitors. The ENA imagers are placed on actuators to provide two-dimensional, time-of-flight measurements. Additional details are available elsewhere (Goldstein & McComas, 2013, 2018; A M Keesee, Chen, Scime, & Lui, 2014).

Two-dimensional ion temperature maps (e.g., Figure 1a) were created using the methods of ion temperature calculation and line-of-sight (LOS) projection that have been previously validated with in situ measurements (A. Keesee, Scime, Zaniewski, & Katus, 2019; A M Keesee et al., 2014; A M. Keesee, Scime, & Moldwin, 2008; Scime et al., 2002). Once the ENA flux and orbit data were obtained as a function of date and spacecraft, two procedures were implemented to maintain data quality. The first procedure removed all intervals with an actuator pointing uncertainty above 4°. Second, intervals when the instrument was facing the sun were removed. As described previously, the ENA flux is projected to a 160 × 160 grid with 0.5 R_E resolution

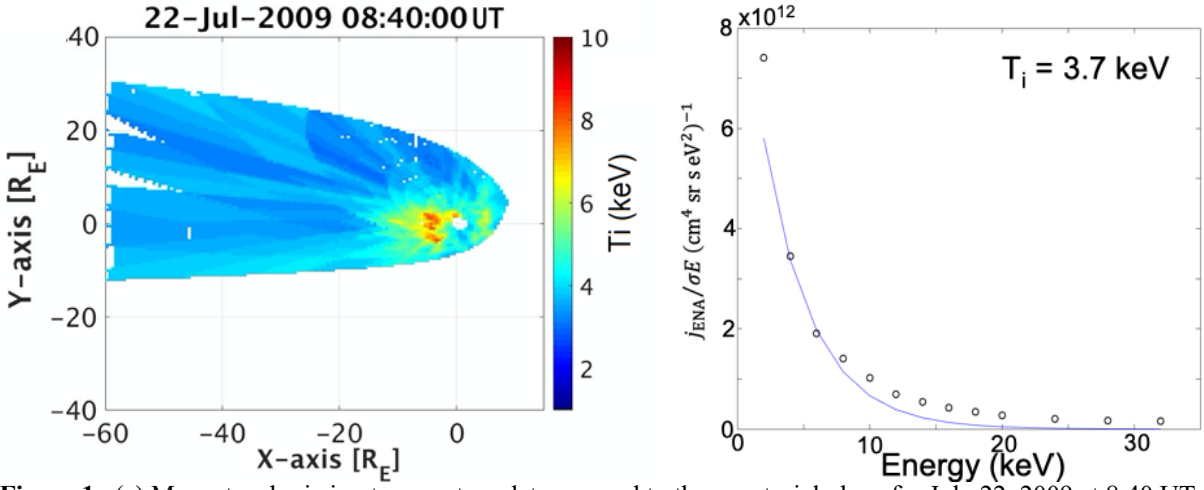

Figure 1. (a) Magnetospheric ion temperature data mapped to the equatorial plane for July 22, 2009 at 8:40 UT. (b) Energetic neutral atom flux versus energy (circles) and a fit to the data (solid line) using Eq. (2) for June 1, 2013 at 06:00 UT at x = – 5 R_E and y = 0 R_E, resulting in a temperature of 3.7 keV.

extending from -60 R_E to 20 R_E in the x-direction and -40 R_E to 40 R_E in the y-direction using GSM coordinates (A. M. Keesee, Elfritz, McComas, & Scime, 2012). A fit assuming a Maxwellian parent ion distribution is used to calculate the ion temperature at each grid location (an example is shown in Figure 1b). Some deviation from a strict Maxwellian distribution at low ENA energies (< 5 keV) typically occurs, particularly due to contributions from oxygen ENAs, and is evident in Figure 1b.

2.3 Database format and metadata

The data are converted to CDF with all descriptions and metadata in Extensible Markup Language (XML) according to the Space Physics Archive Search Model. The metadata include the date, time, the spacecraft position, and the name (TWINS-1 or TWINS-2) of the satellite used to produce the time step.

3 Example analysis

To demonstrate the utility of the database, we have conducted a preliminary analysis of the average plasma sheet ion temperature during storm time evolution as a function of solar wind

parameters. The average plasma sheet ion temperature is calculated by selecting the region -60 $R_E < x < -5$ R_E and 20:00 < MLT < 4:00 from the 10-minute averaged temperature maps, shown in Figure 2a. Using MLT results in varying coverage along the *y*-axis that increases with distance from the Earth, with -10 $R_E < y < 10$ R_E at geosynchronous orbit. Figure 2b shows the average ion temperatures for July 21-25, 2009, with the average from the individual satellites shown in the 2nd and 3rd panels. Those values are also shown in the first panel in blue for TWINS 1 and red for TWINS 2, with the final calculated average in yellow. When data from only one satellite is available, the average plasma sheet ion temperature from that satellite is used for the final average. When there are overlapping intervals between the two TWINS satellites, an average map is first created by calculating the average temperature in each equatorial plane bin from the individual satellite maps, then the average over the plasma sheet region from the average map is calculated. Note that if one satellite has a larger FOV, the equatorial plane bins that are only populated in the map for that satellite will take on the value from that satellite in the average map, thus it will have more weight in the plasma sheet average. This can be seen when considering the interval on July 22, 2009 from 00:00 UT to 1:40 UT. In the top panel of Figure 2b, the yellow final average lies closer to the red TWINS 2 average than the blue TWINS 1 average. The ion temperature maps from four of the 10-minute averages during this interval are shown in Figure 2c, with the rows showing the maps for TWINS 1, TWINS 2, and the averaged map, respectively. It can be seen that the larger FOV of TWINS 2 during this interval contributes more bins to the plasma sheet area than TWINS 1, so the final average (yellow in Fig. 2b) is dominated by contributions from TWINS 2 and will, therefore, be closer to the average calculated from the TWINS 2 map (red in Fig. 2b). This comparison, thus, gives some quantification of the error of the average ion temperature, which tends to be less than +/- 2 keV.

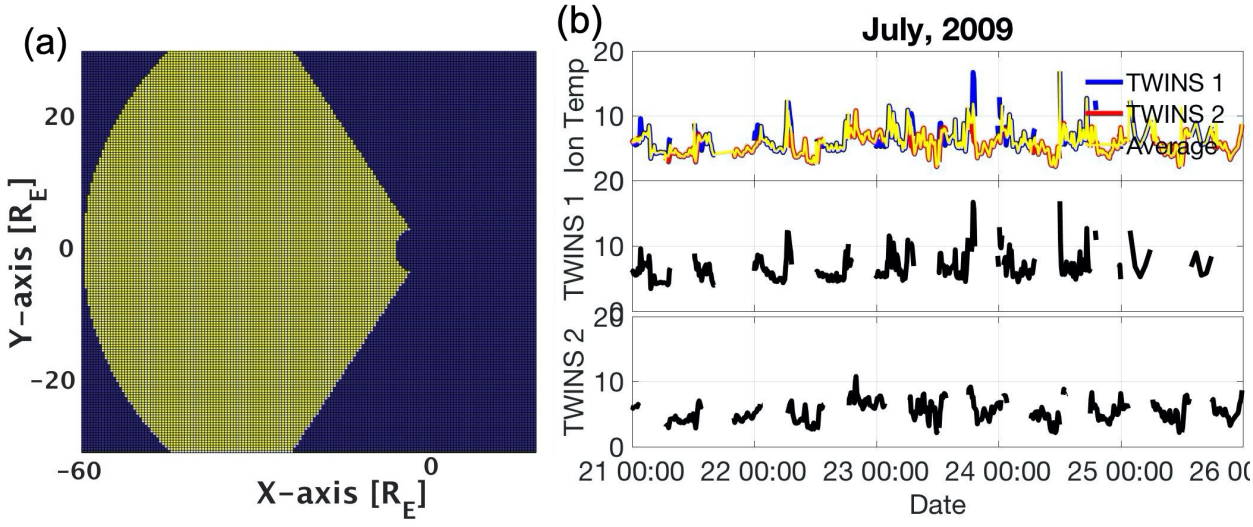

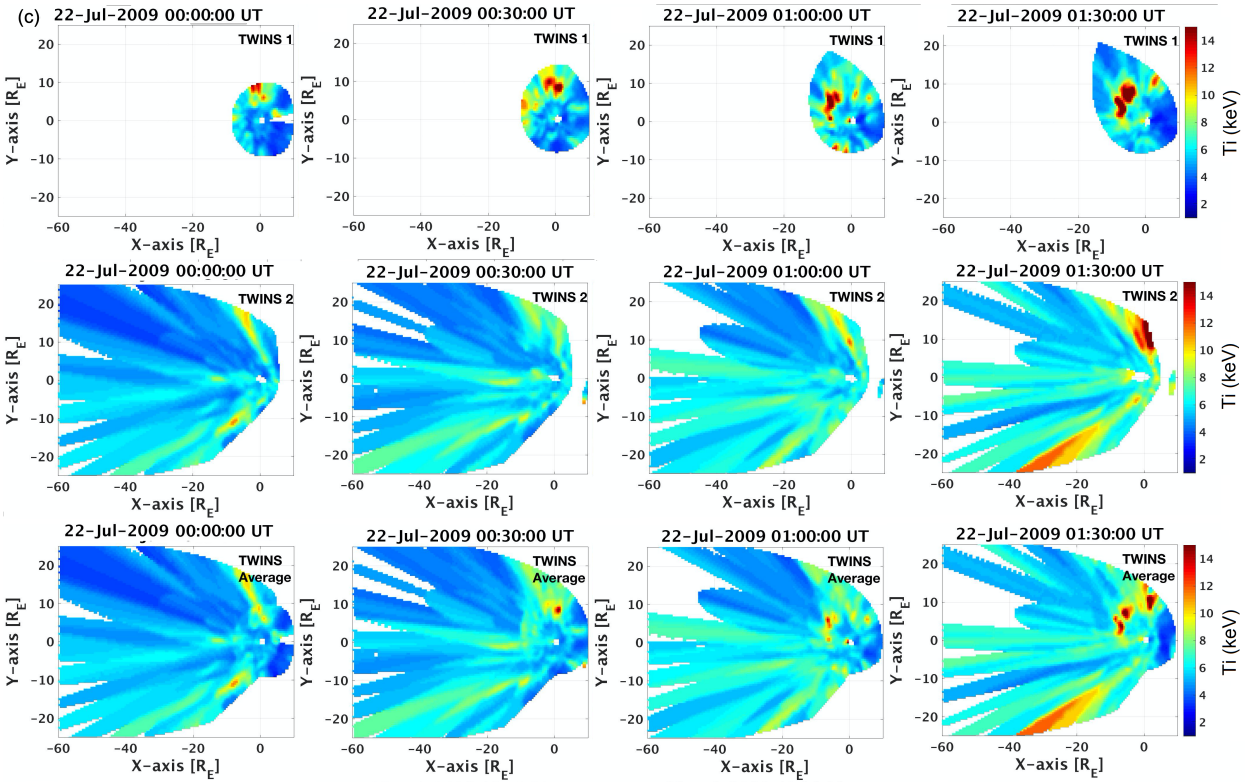

149

150 **Figure 2.** Calculation of the average plasma sheet ion temperature. a) The plasma sheet region
151 used to calculate the ion temperature average is shown in yellow. b) Average ion temperature in
152 the plasma sheet calculated from TWINS 1 (blue in top panel and second panel) and TWINS 2
153 (red in top panel and third panel) and the final average (yellow in top panel) that is calculated
154 from an averaged map for overlapping intervals. c) Four 10-minute averages (columns) during an
155 overlapping interval with the TWINS 1 (top row), TWINS 2 (middle row), and averaged map
156 (bottom row) shown.

157 The 10-minute averages of solar wind dynamic pressure, IMF, velocity magnitude, AE,
158 and Dst are obtained from OmniWeb for comparison. Using these data, we have found a trend
159 where the plasma sheet temperature drops following a strong southward gradient in the IMF B_z,
160 and the temperature remains low until the B_z recovers. Two case studies are described here, and
161 we plan to conduct a more comprehensive study of the entire database, including a superposed
162 epoch analysis as a function of storm strength and driver, in the near future.

163 In the first case for the July 22, 2009 storm, there are two ion temperature drops
164 associated with negative IMF B_z gradients. Figure 3 shows the average plasma sheet ion
165 temperature along with IMF and solar wind conditions and the AE and Dst indices. The 10-
166 minute averaged ion temperature maps are shown at 30-minute intervals in Figure 4 for 3:30-
167 13:00 UT on July 22. The ion temperature increases over 5:00-6:30 UT on July 22nd, near the
168 peak of the storm, following an increase in pressure and concurrent with a northward turning and
169 increase in B_z. The temperature drops around 8:00 UT concurrent with a strong southward B_z
170 turning. B_z returns northward around 9:00 UT, followed by a smaller ion temperature increase.
171 The B_z turns southward again around 10:00 UT, followed by a second drop in the plasma sheet
172 temperature that remains low for a couple of hours. The first southward B_z turning results in a

large southward B_z compared to a much smaller magnitude for the second turning, but the average temperature is lower in the second interval which has a stronger B_z gradient. It can be seen in Figure 4 that there is a region of ~6 keV ions in the plasma sheet near the Earth during the first low temperature interval (Figs. 4j-m), but barely any enhanced regions in the second (Figs. 4o-s), resulting in that lower average temperature. A peak in the AE index following the large southward B_z turning around 8:00 UT indicates substorm activity and the Dst index has a second dip following this time as well. Thus, the first southward turning appears to have resulted in injections from the plasma sheet to the inner magnetosphere. The short northward turning only allowed for partial recovery and heating of the plasma sheet prior to the second, smaller southward B_z turning. The ion temperature returned to average values of ~ 5 keV around 13:00 UT after the B_z had been near zero for several hours.

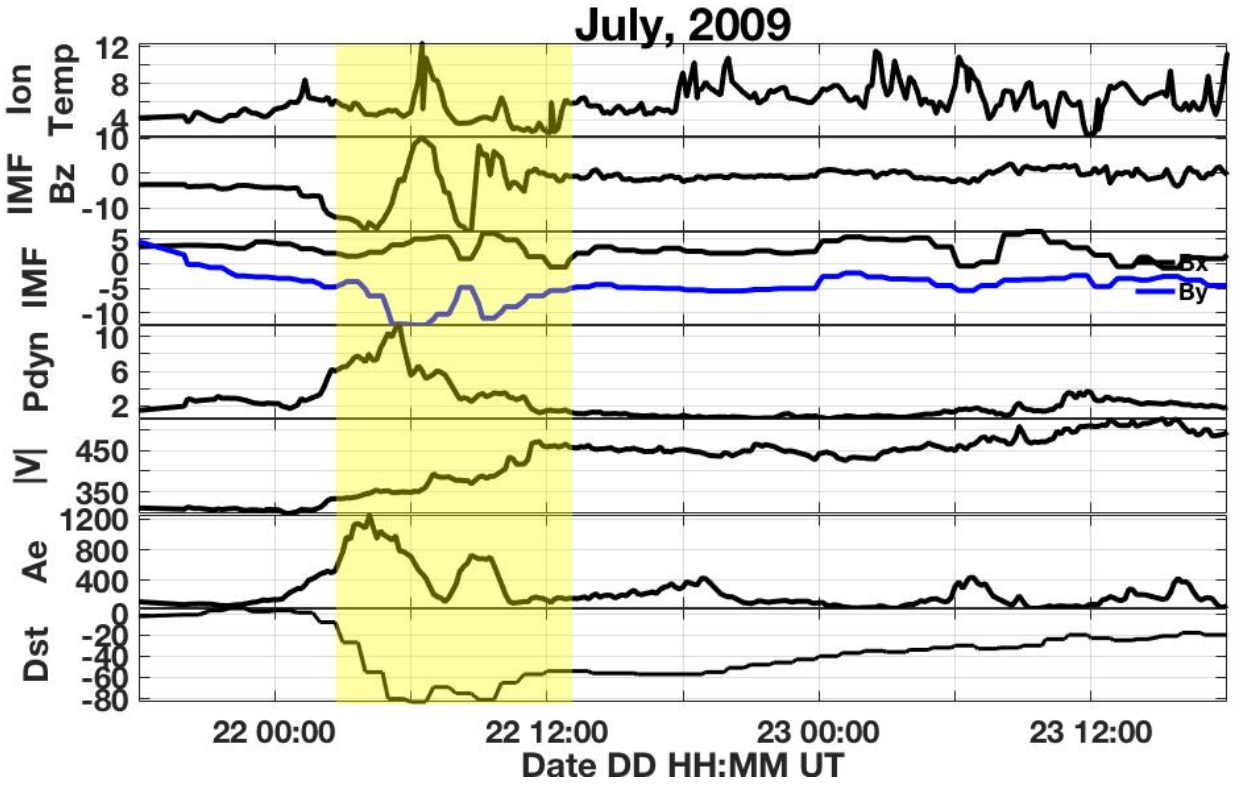

Figure 3. TWINS-derived spatially-averaged plasma sheet ion temperature at 10-minute averaged intervals (keV), and OMNIWeb obtained values averaged at 10-minute intervals of IMF B_z (nT), B_x (nT), B_y (nT), dynamic Pressure (nPa), velocity magnitude (km/s), AE index (nT), and Dst index (nT) as a function of time for July 21-23, 2009. The shaded area indicates the interval of interest, 3:30 UT-13:00 UT, as described in the text.

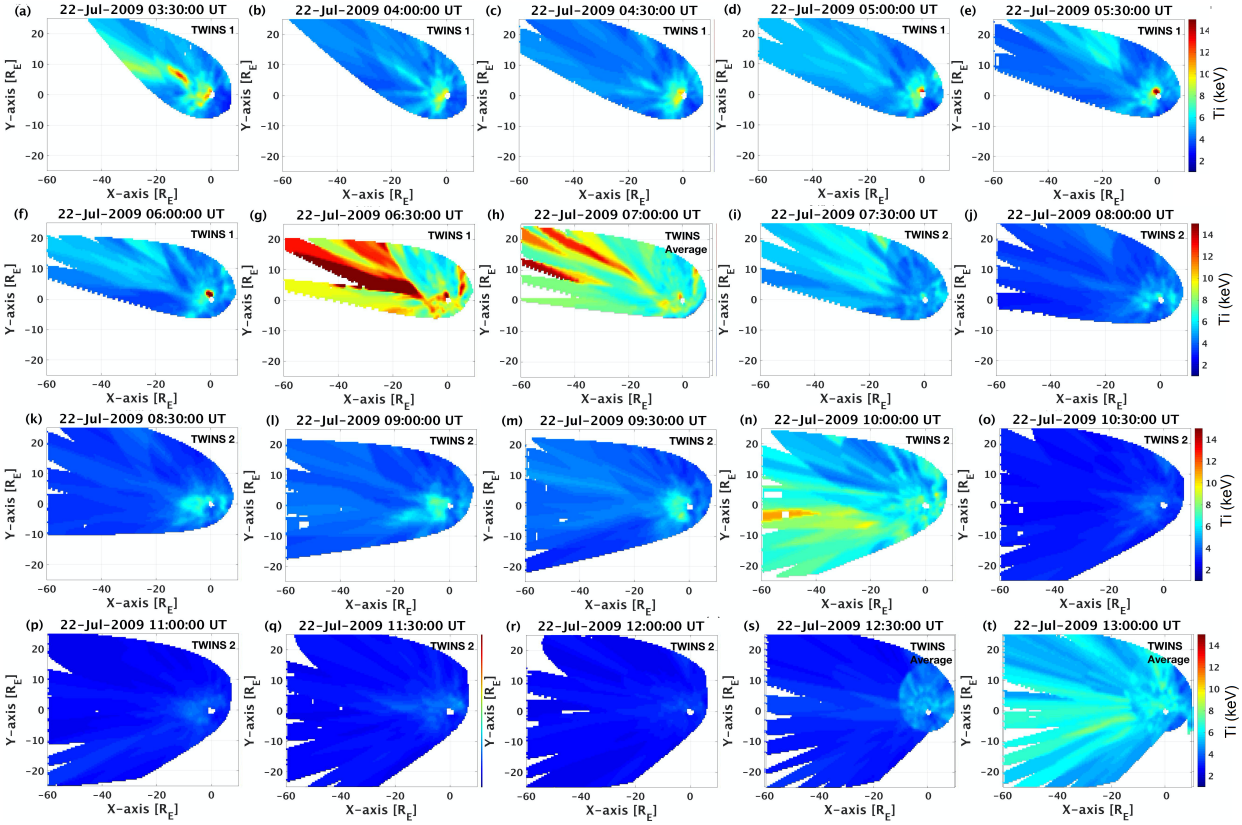

Figure 4. TWINS-derived ion temperature maps. The sequence shows a 10-minute average every 30 minutes from 3:30 UT-13:00 UT (shaded area of Fig. 3) on July 22, 2009. Each map indicates whether it is calculated from TWINS 1, TWINS 2, or an average.

We do note that the first ion temperature increase and beginning of the subsequent temperature drop occur during an interval of overlap between the two TWINS satellites, as does the final temperature recovery. The orbits of the satellites are shown in Figure 5 and the overlapping temperature maps are shown in Figure 6, including the individual maps from TWINS 1 and TWINS 2 as well as the averaged map, so that we may examine them more closely. The first overlapping interval lasts 6:30 UT-7:30 UT where TWINS 1 is descending toward perigee and TWINS 2 is ascending toward apogee. It can be seen from Figure 5 that the satellites are relatively close to each other during this interval, resulting in the similarly shaped FOVs in Figs. 6 a-d. The average temperature observed by TWINS 1 is quite a bit higher than TWINS 2 for most of this overlapping interval (Figs. 6a-c), resulting in the large peak seen in Figure 3. It is possible for in situ particle contamination to occur as the satellites are lower in their orbits, but the TWINS Lyman-alpha detectors do not indicate higher than usual counts during this interval (not shown). Since this temperature peak occurs during the peak of the storm, it is likely that TWINS 1 observes energetic particles in the inner magnetosphere that are erroneously mapped to the tail. However, TWINS 2 does also observe an increase in temperatures over this interval, just with a reduced magnitude, and the agreement in the final overlapping interval (Fig. 6d) is good. Similarly, another overlap occurs over ~ 12:10 UT – 13:30 UT (every other 10 minute interval is shown in Figs. 6e-h), now with TWINS 1 ascending toward apogee and TWINS 2 descending toward perigee. During this interval, the satellites are in

quite different locations, as seen in Fig. 5, resulting in very different FOVs, as seen in Figs. 6 e-h. However, there is much better agreement in average temperature between the two satellites over most of this interval, indicating that the mappings of the increased temperatures observed at this time are mutually consistent, though the exact timing is unclear as seen in the difference between the satellites early in this interval in Fig. 6e. The takeaway from this comparison is that the timing and intensity of the temperature variations will have to be carefully considered, especially during intervals when the satellites are lower in their orbits.

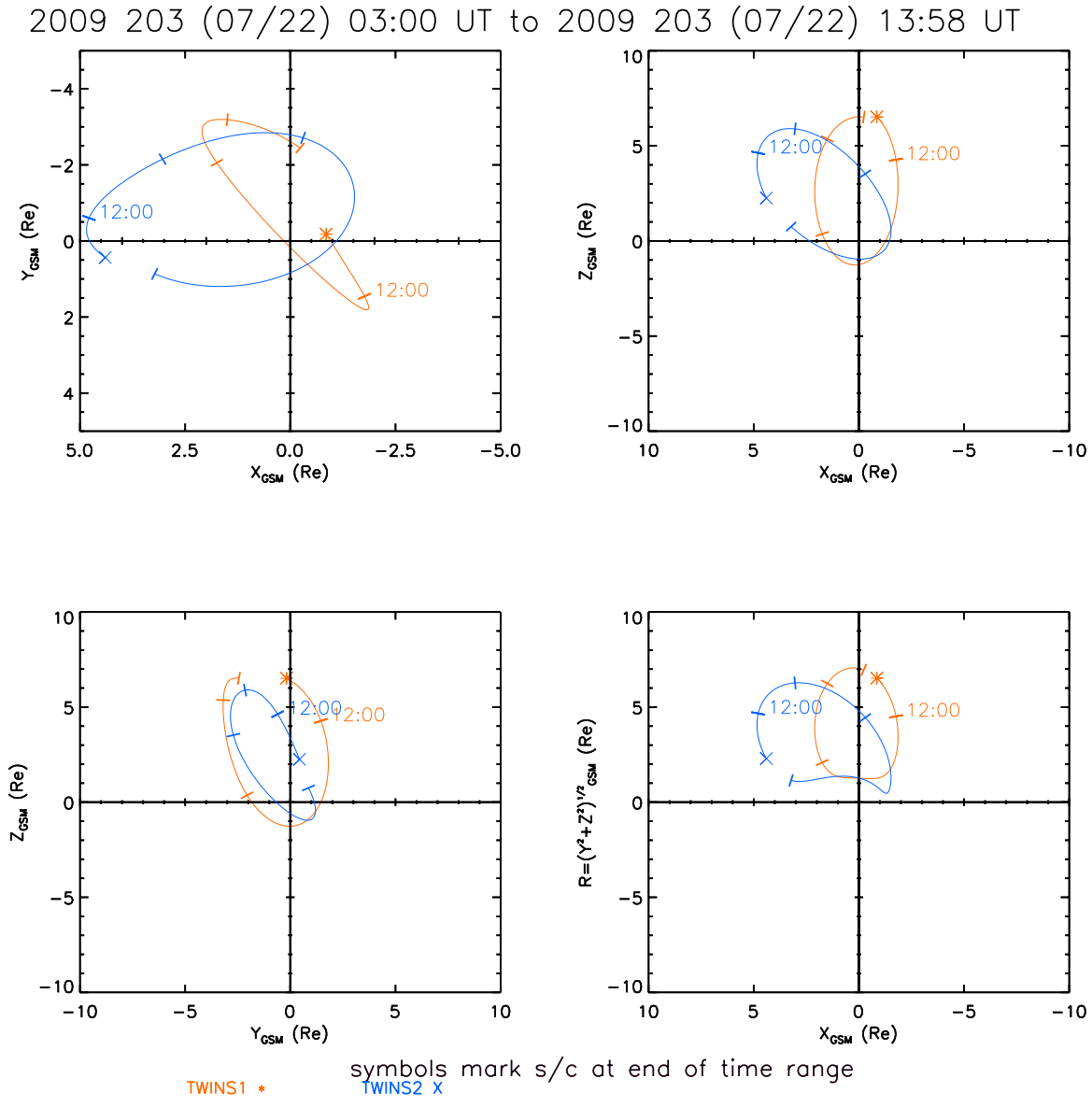

Figure 5. Orbital plots from SSCweb for TWINS 1 (red *) and TWINS 2 (blue X) for July 22, 2009 3:00 UT – 14:00 UT. Tick marks are every 3 hours and the symbols mark the location at the end of the interval.

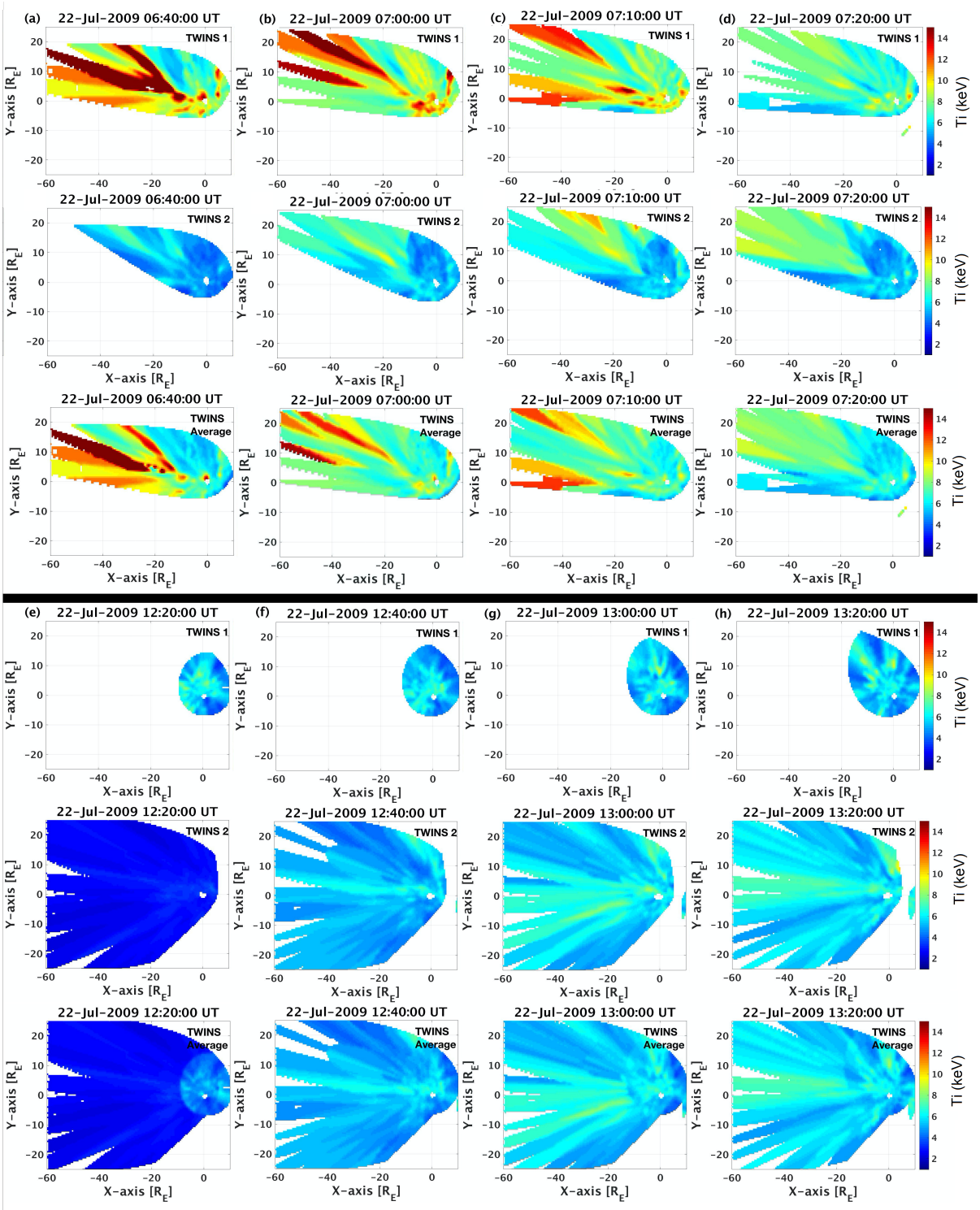

Figure 6. Ion temperature maps for TWINS 1 and TWINS 2 during intervals of overlapping coverage on July 22, 2009, including (a-d) 6:40 UT – 7:30 UT and (e-h) every other 10 minute interval over 12:20 UT-13:30 UT.

The second case, for the storm on February 15, 2010, is shown in Figures 7 and 8. In Figure 7, the ion temperature increases starting after 12:00 UT on February 15th while the B_z is moderately southward, but drops, though somewhat gradually, after the sharp negative B_z gradient just after ~18:00 UT. After remaining low for several hours during the peak of the storm, the ion temperature increases again toward the end of the 15th with the recovery of B_z. Like the July case, these drops occur near the peak in Dst. In contrast to the July case, the B_z remains mostly southward for the entire interval. We also note a drop in temperature that occurs ~ 4:00-7:00 UT on the 16th. This occurs while the IMF Bz remains at a constant, slightly southward value, though there are changes in the IMF By and Bx and the dynamic pressure and solar wind velocity are decreasing, which all precedes an inflection point in the Dst index. Further study is needed to understand the varying causes of these temperature drops.

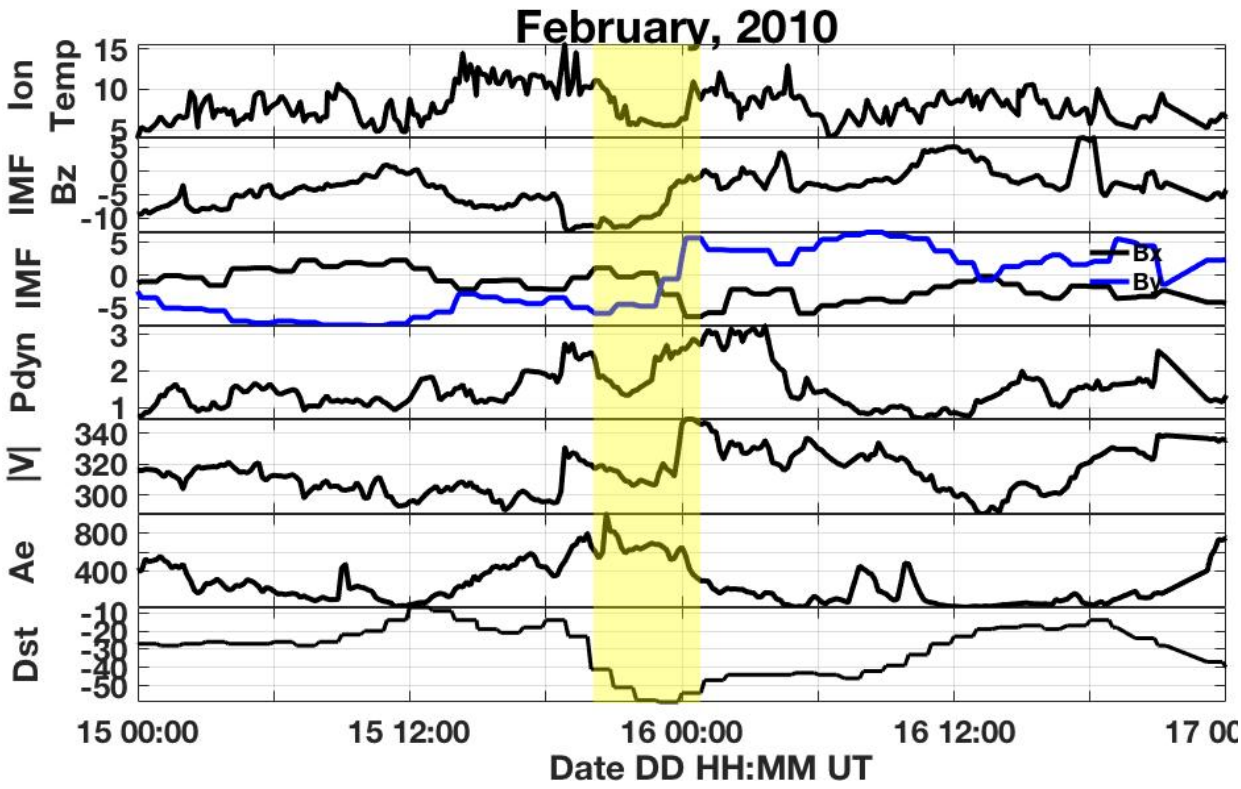

Figure 7. TWINS-derived spatially-averaged plasma sheet ion temperature at 10-minute averaged intervals (keV), and OMNIWeb obtained values averaged at 10-minute intervals of IMF B_z (nT), B_x (nT), B_y (nT), dynamic Pressure (nPa), velocity magnitude (km/s), AE index (nT), and Dst index (nT) as a function of time for February 15-16, 2010. The shaded area indicates the interval of interest, 20:00 UT on February 15, 2010 – 00:30 UT on February 16, 2010, as described in the text.

In Figure 8, the ion temperature maps from 20:00 UT on February 15, 2010 to 00:30 UT on February 16, 2010 are shown at 30-minute intervals. A temperature map was not created for

the 22:30 UT interval due to actuator pointing uncertainty > 4°, so the 22:40 UT interval is shown instead (Fig. 8f). At the beginning of the interval, there appear to be higher temperature regions across all MLT that all consistently decrease in temperature. The increase starting in Figure 9i is dominated by the dusk side of the plasma sheet. This latter behavior is typical of the gradient curvature drift observed during intervals without significant external driving (A M Keesee et al., 2011). However, the solar wind velocity has a sharp increase during this interval, which is correlated with increasing plasma sheet ion temperatures (Borovsky et al., 1998).

This interval includes an overlap of TWINS 1 and TWINS 2 data as TWINS 2 was traveling Earthward in its orbit and TWINS 1 was traveling toward apogee. The changing field of view caused by the orbital motion of the spacecraft is apparent in this figure as TWINS 2 is already low, resulting in a smaller field of view that continues to decrease (Figs. 8a-d). The overlapping interval occurs ~20:50 UT to 22:10 UT, but only one of the three panels (Figs. 8c-e) during this interval has an average map. The ion temperature maps during a portion of the overlapping interval (20:50 UT – 21:30 UT) are shown in Figure 9 to understand why this is the case. The first interval (Fig. 9a) has maps from both TWINS 1 and TWINS 2, so an average map is calculated (bottom panel). However, for the remaining intervals, one of the satellites has actuator pointing uncertainty > 4°, so only one map is available, and no average map is calculated. However, we can see from Figure 9 and the average in Fig. 8e that the temperature decrease over this interval is consistent in both satellites.

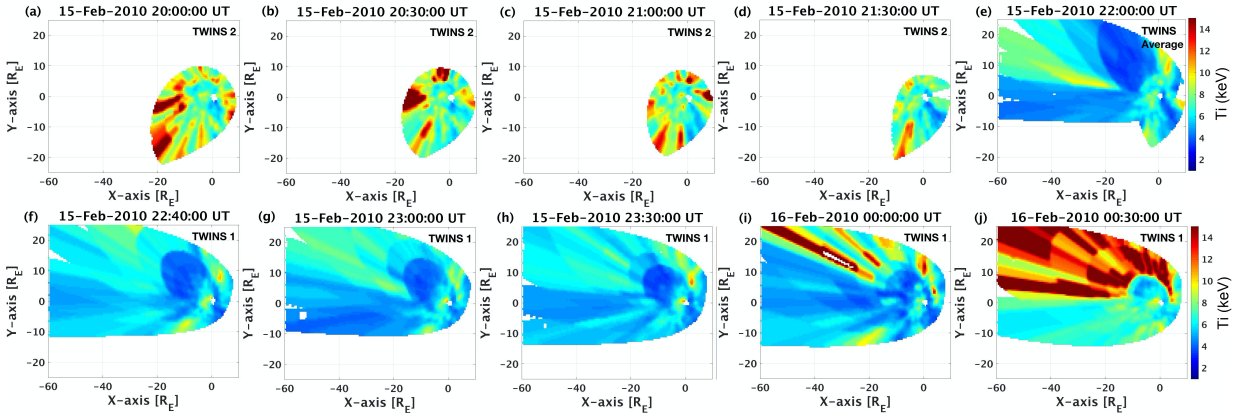

Figure 8. TWINS-derived ion temperature maps. The sequence shows 10-minute averages every 30 minutes from 20:00 UT on February 15, 2010 to 00:30 UT on February 16, 2010 (shaded area in Fig. 7). Note, there is no map for the 22:30 UT interval so the 22:40 UT interval is shown instead.

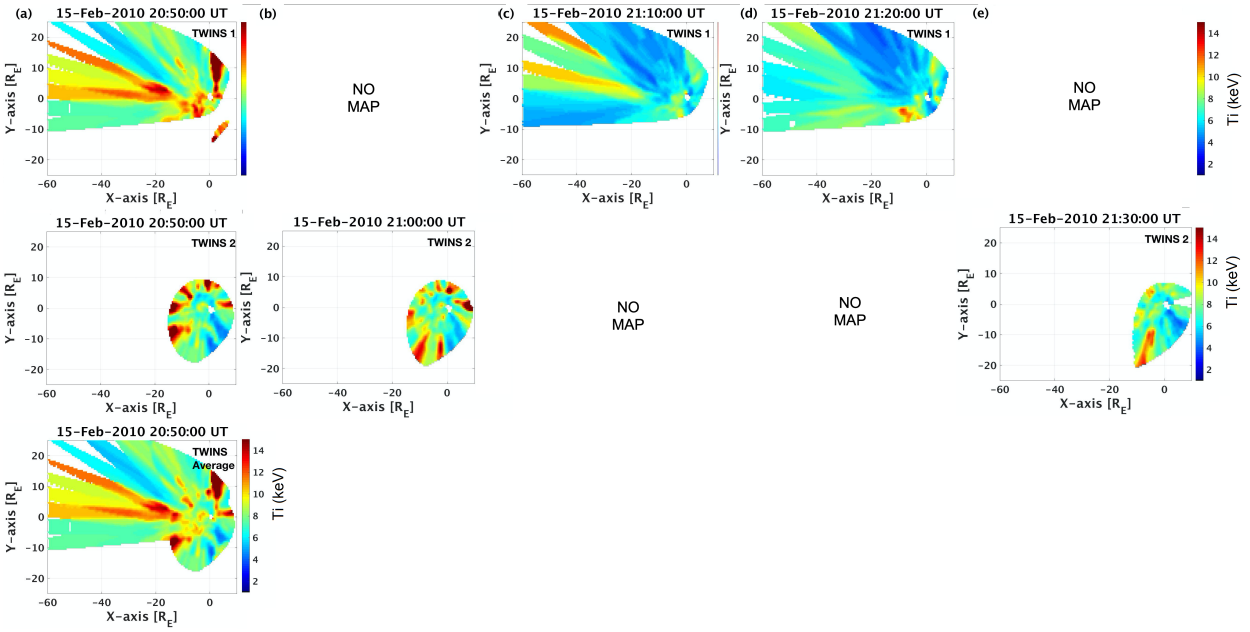

Figure 9. Ion temperature maps during overlap between TWINS 1 and TWINS 2 for 20:50 UT to 21:30 UT on February 15, 2010. The top row is from TWINS 1, second row from TWINS 2, and bottom row is the average map. Several intervals have no maps due to actuator pointing uncertainty > 4°, thus no average is calculated during those intervals.

4 Discussion

A strong or prolonged northward IMF allows energetic electrons to collect in the plasma sheet. A southward turning of the IMF B_z then triggers magnetic reconnection in the tail, resulting in the injection of hot ions from the plasma sheet to the inner magnetosphere. The trend of the plasma sheet ion temperature drop is an indication of this "clearing" of the hot ions from the plasma sheet. There are AE peaks that occur around the time of the ion temperature drops for both cases (Figs. 3 and 7) indicating substorm activity. The strength of the B_z temporal gradient is an important factor in triggering this clearing. Slow, gradual southward turning does not result in the lower temperatures. As described previously for the July 2009 storm, the second interval has a stronger temporal gradient and results in lower plasma sheet temperatures. It can also be seen in the February 2010 case (Fig. 7), that a very weak southward gradient over ~12:00-18:00 UT on February 15th did not result in an ion temperature drop, but rather an increase, while the sharp gradient does result in the ion temperature drop. The sharp gradients in B_z are an indication of the solar wind structure, which depends on the storm driver. The July storm was driven by a co-rotating interaction region (CIR) while the February storm was driven by a coronal mass ejection (CME) (Amy M. Keesee & Scime, 2015). Further study is needed to better understand these differences that influence the plasma sheet temperature. The strength of the IMF B_y may also play a role. Penetration of the IMF B_y into the magnetosphere enhances the cross-tail B_y, thus increasing Earthward convection. A strong IMF B_y is seen in these intervals, with a change in direction occurring at a similar time as the end of the interval of low plasma sheet

304 temperatures. Thus, when the B_y weakens, so does the convection, enabling the plasma sheet to
305 refill with hotter ions.

306

307 **5 Conclusions**

308 We have calculated equatorial ion temperature maps at 10-minute cadence for 90
309 geomagnetic storms using TWINS ENA data. This database of ion temperature maps has been
310 made available at CDAWeb in cdf format with the necessary metadata for community use in
311 modeling and other magnetospheric studies. As an example, we have conducted a preliminary
312 analysis of plasma sheet ion temperature trends in relation to solar wind dynamics. We have
313 found that a drop in ion temperatures occurs in conjunction with strong southward gradient in
314 IMF B_z in several intervals. This is consistent with the hot ions being injected during a substorm
315 triggered by the southward increase in certain cases, leaving a cooler plasma sheet behind.
316 Further studies of this phenomenon will be conducted.

317

318

319 **Acknowledgments, Samples, and Data**

320 TWINS data, both ENA format (TWINSX_L1_IMAGER) and temperature maps
321 (TWINS_M2_ENA) described in this paper, are available at
322 https://cdaweb.gsfc.nasa.gov/index.html/.

323 **References**

324 Angelopoulos, V., Kennel, C. F., Kivelson, M. G., Walker, R. J., & Paschmann, G. (1992).
325 Bursty Bulk Flows in the Inner Central Plasma Sheet. *Journal of Geophysical Research*,
326 *97*(A4), 4027–4039.

327 Borovsky, J. E., Thomsen, M. F., & Elphic, R. C. (1998). The driving of the plasma sheet by the
328 solar wind layer. *Journal of Geophysical Research*, *103*, 17,617-17,639.

329 Chen, M. W., Lemon, C. L., Guild, T. B., Keesee, A. M., Lui, A., Goldstein, J., … Anderson, P.
330 C. (2015). Effects of modeled ionospheric conductance and electron loss on self-consistent
331 ring current simulations during the 5-7 April 2010 storm. *Journal of Geophysical Research:*
332 *Space Physics*, *120*, 5355–5376. https://doi.org/10.1002/2015JA021285

333 Elfritz, J., Keesee, A., Buzulukova, N., Fok, M.-C., & Scime, E. E. (2014). First results using
334 TWINS-derived ion temperature boundary conditions in CRCM. *Journal of Geophysical*
335 *Research*, *119*, 3345–3361. https://doi.org/10.1002/2013JA019555

336 Freeman, R. L., & Jones, E. M. (1974). Atomic Collision Processes in Plasma Physics
337 Experiments. *Culham Laboratory Report*, *CLM-R 137*.

338 Goldstein, J., & McComas, D. J. (2013). Five years of stereo magnetospheric imaging by
339 TWINS. *Space Science Reviews*, *180*(1–4), 39–70. https://doi.org/10.1007/s11214-013-
340 0012-8

Goldstein, J., & McComas, D. J. (2018). The Big Picture: Imaging of the Global Geospace Environment by the TWINS Mission. *Reviews of Geophysics*, *56*(1), 251–277. https://doi.org/10.1002/2017RG000583

Hutchinson, I. H. (1987). *Principles of Plasma Diagnostics*. Cambridge: Cambridge Univ. Press.

Katus, R. M., Liemohn, M. W., Ionides, E., Ilie, R., & Welling, D. T. (2015). Statistical analysis of the geomagnetic response to different solar wind drivers and the dependence on storm intensity. *Journal of Geophysical Research: Space Physics*, *120*, 310–327. https://doi.org/10.1002/2014JA020712

Keesee, A. M., Elfritz, J. G., McComas, D. J., & Scime, E. E. (2012). Inner magnetosphere convection and magnetotail structure of hot ions imaged by ENA during a HSS-driven storm. *Journal of Geophysical Research*, *117*, A00L06. https://doi.org/10.1029/2011JA017319

Keesee, A., Scime, E., Zaniewski, A., & Katus, R. (2019). 2D Ion Temperature Maps from TWINS ENA data: IDL scripts. UNH Scholars' Repository. https://doi.org/https://dx.doi.org/10.34051/c/2019.1

Keesee, A M, Buzulukova, N., Goldstein, J., Mccomas, D. J., Scime, E. E., Spence, H., … Tallaksen, K. (2011). Remote observations of ion temperatures in the quiet time magnetosphere. *Geophysical Research Letters*, *38*, 1–5. https://doi.org/10.1029/2010GL045987

Keesee, A M, Chen, M. W., Scime, E. E., & Lui, A. T. Y. (2014). Regions of ion energization observed during the Galaxy-15 substorm with TWINS. *Journal of Geophysical Research: Space Physics*, *119*, 8274–8287. https://doi.org/10.1002/2014JA020466

Keesee, Amy M., & Scime, E. E. (2015). Database of ion temperature maps during geomagnetic storms. *Earth and Space Science*, *2*, 39–46. https://doi.org/10.1002/2014EA000061

Keesee, Amy M., Scime, E., & Moldwin, M. B. (2008). Remote measurements of ion temperatures in the terrestrial magnetotail. *Journal of Geophysical Research*, *113*, A00A03. https://doi.org/10.1029/2008JA013130

McComas, D. J., Allegrini, F., Baldonado, J., Blake, B., Brandt, P. C., Burch, J., … Zoennchen, J. (2009). The Two Wide-angle Imaging Neutral-atom Spectrometers (TWINS) NASA Mission-of-Opportunity. *Space Science Reviews*, *142*(1–4), 157–231. https://doi.org/10.1007/s11214-008-9467-4

Ozeke, L. G., & Mann, I. R. (2008). Energization of radiation belt electrons by ring current ion driven ULF waves. *Journal of Geophysical Research: Space Physics*, *113*(2), 4–11. https://doi.org/10.1029/2007JA012468

Scime, E. E., Keesee, A. M., Jahn, J.-M., Kline, J. L., Pollock, C. J., & Thomsen, M. (2002). Remote ion temperature measurements of Earth's magnetosphere: Medium energy neutral atom (MENA) images. *Geophysical Research Letters*, *29*(10), 1438. Retrieved from http://www.agu.org/pubs/crossref/2002/2001GL013994.shtml

Spence, H. E., & Kivelson, M. (1993). Contributions of the low-latitude boundary layer to the finite width magnetotail convection model. *Journal of Geophysical Research*, *98*, 15487–15496. Retrieved from http://www.igpp.ucla.edu/people/mkivelson/Publications/144-

93JA01531.pdf

Takahashi, N., Seki, K., Amano, T., Miyoshi, Y., & Yamakawa, T. (2019). Excitation of storm-time Pc5 ULF waves by ring current ions based on the drift-kinetic simulation. *Geophysical Research Letters*, 1911–1918. https://doi.org/10.1029/2018gl081573

Tsyganenko, N. A., & Mukai, T. (2003). Tail plasma sheet models derived from Geotail particle data. *Journal of Geophysical Research*, *108*(A3), 1–15. https://doi.org/10.1029/2002JA009707

Wiltberger, M., Merkin, V., Lyon, J. G., & Ohtani, S. (2015). High-resolution global magnetohydrodynamic simulation of bursty bulk flows. *Journal of Geophysical Research : Space Physics*, *120*, 4555–4566. https://doi.org/10.1002/2015JA021080

Zhao, H., Baker, D. N., Li, X., Jaynes, A. N., & Kanekal, S. G. (2019). The Effects of Geomagnetic Storms and Solar Wind Conditions on the Ultrarelativistic Electron Flux Enhancements. *Journal of Geophysical Research: Space Physics*, *124*(3), 1948–1965. https://doi.org/10.1029/2018JA026257